AGU PUBLICATIONS

JGR

Journal of Geophysical Research: Oceans

RESEARCH ARTICLE

10.1002/2015JC010884

Observational validation of the diffusive convection flux laws in the Amundsen Basin, Arctic Ocean

John D. Guthrie[1], Ilker Fer[2], and James Morison[1]

[1]Polar Science Center, Applied Physics Laboratory, University of Washington, Seattle, WA, USA, [2]Geophysical Institute, University of Bergen and Bjerknes Centre for Climate Research, Bergen, Norway

Key Points:
- Laboratory flux laws of diffusive convection agree well with microstructure observations
- Observations support a downward revision of the convective exponent from 1/3 to 0.29
- Double diffusive heat fluxes could account for 2 TW of heat loss from the Atlantic Water

Correspondence to:
J. Guthrie,
guthriej@apl.washington.edu.

Citation:
Guthrie, J. D., I. Fer, and J. Morison (2015), Observational validation of the diffusive convection flux laws in the Amundsen Basin, Arctic Ocean, *J. Geophys. Res. Oceans*, *120*, 7880–7896, doi:10.1002/2015JC010884.

Received 27 MAR 2015
Accepted 12 NOV 2015
Accepted article online 18 NOV 2015
Published online 12 DEC 2015

Abstract The low levels of mechanically driven mixing in many regions of the Arctic Ocean make double diffusive convection virtually the only mechanism for moving heat up from the core of Atlantic Water towards the surface. In an attempt to quantify double diffusive heat fluxes in the Arctic Ocean, a temperature microstructure experiment was performed as a part of the North Pole Environmental Observatory (NPEO) 2013 field season from the drifting ice station Barneo located in the Amundsen Basin near the Lomonosov Ridge (89.5°N, 75°W). A diffusive convective thermohaline staircase was present between 150 and 250 m in nearly all of the profiles. Typical vertical heat fluxes across the high-gradient interfaces were consistently small, O(10^{-1}) W m^{-2}. Our experiment was designed to resolve the staircase and differed from earlier Arctic studies that utilized inadequate instrumentation or sampling. Our measured fluxes from temperature microstructure agree well with the laboratory derived flux laws compared to previous studies, which could find agreement only to within a factor of two to four. Correlations between measured and parameterized heat fluxes are slightly higher when using the more recent *Flanagan et al.* [2013] laboratory derivation than the more commonly used derivation presented in *Kelley* [1990]. Nusselt versus Rayleigh number scaling reveals the convective exponent, η, to be closer to 0.29 as predicted by recent numerical simulations of single-component convection rather than the canonical 1/3 assumed for double diffusion. However, the exponent appears to be sensitive to how convective layer height is defined.

1. Introduction

The Atlantic Water (AW) layer persists throughout the Arctic Ocean as a subsurface temperature maximum (0.5–3°C), typically found at 200–300 m depths. The AW enters the Arctic Ocean through Fram Strait and circulates cyclonically around the basin with the Siberian continental slope on its right. Recirculation pathways of the AW exist along the southern side of the Nansen-Gakkel Ridge in the Nansen Basin as well as along the Eurasian side of the Lomonosov Ridge in the Amundsen Basin. Slightly cooler AW continues to follow bathymetry into the Makarov and Canada basins [*Rudels et al.*, 2004].

Starting at the surface, vertical profiles of water properties in the Amundsen Basin (AB) of the Arctic Ocean nominally consist of a low-salinity, cold mixed layer; a cold, saltier (cold halocline) layer and below, a warm, salty AW layer. The positive temperature and salinity gradients with depth above the AW core result in most of the AB being susceptible to the diffusive convective form of double diffusion (DDC) [*Kelley et al.* 2003]. A similar situation applies to some extent for the majority of the Arctic Ocean. AW temperature maxima in the AB range from 1.0 to 1.3°C, and salinity maxima are usually around 34.8. The commonly used form of the density ratio for DDC, $R_\rho = \beta\Delta S/\alpha\Delta T$, is a measure of the susceptibility of the water column to double diffusion, and DDC is expected for $1 < R_\rho < 10$. Here, β is the haline contraction coefficient, and α is the thermal expansion coefficient of seawater. Please note that for the salt fingering regime R_ρ is typically defined inversely. Through the thermocline in the AB, R_ρ usually ranges between 3 and 4 and is slightly lower than in the Canada Basin overall [*Padman and Dillon*, 1987; *Sirevaag and Fer*, 2012; *Timmermans et al.*, 2008].

In the deep basins of the Arctic Ocean, turbulence levels are low. The strength of turbulence is typically quantified by the dissipation of turbulent kinetic energy, ε, obtained by integrating the small-scale shear variance spectrum measured by airfoil shear probes on microstructure profilers. Away from topographic features, previous shear microstructure measurements in the Arctic Ocean have had trouble resolving the low levels of turbulence. During the Arctic Internal Wave Experiment (AIWEX) in the Canada Basin in 1985,

Padman and Dillon [1987] found ε to be near the noise level of their instrument throughout the experiment. More recently, *Fer* [2009] and *Sirevaag and Fer* [2012] report diapycnal diffusivities of O(10^{-6}) m^2s^{-1} at depths less than 200 m but below that, ε typically falls below the noise level of their instruments. Internal wave energy levels have typically been an order of magnitude or more lower than midlatitude open ocean conditions [*Levine et al*., 1987], and comparisons of historical and recent shear measurements [*Guthrie et al*., 2013] indicate this continues to be true in spite of declines in the ice cover. Thus, nonmechanical mixing regimes like double diffusion potentially dominate the vertical fluxes of heat and salt.

Double diffusion results when an unstable distribution of either temperature or salinity in the water column is compensated by a stable distribution of the other. In the salt fingering (SF) case, salinity is the destabilizing agent as warm, salty water overlies cooler, fresher water. In the diffusive convective case, the opposite occurs as cool, fresh water overlies warm, salty water so that temperature is the destabilizing agent. This sets up an instability that results in the creation of a thermohaline staircase where the water column consists of homogeneous mixed layers separated by thin, high-gradient interfaces in both *T* and *S*.

Based on studies of single-component (e.g., thermal) convection, laboratory laws regarding the fluxes through two-component (*T* and *S*), high-gradient interfaces have been devised based on the density ratio, R_ρ, and the property jumps ΔT and ΔS across the interface. This provides an easily applied method for estimating fluxes in an oceanographic context as actual gradients are much harder to measure, but ΔT and ΔS can be ascertained from standard CTD data.

The original parameterization was presented in *Turner* [1965] based on theories of single-component convection as a scaling in terms of the Nusselt Number (*Nu*), the heat flux relative to conductive heat flux through the layer, and the Rayleigh Number (*Ra*), the strength of the thermal forcing relative to viscous damping of convection:

$$Nu = \frac{F_H}{c_p \rho k_t \left(\frac{\Delta T}{H}\right)}, \tag{1}$$

$$Ra = \frac{g\alpha \Delta T H^3}{\upsilon k_t} \tag{2}$$

$$Nu = cRa^{\eta}. \tag{3}$$

In the above equations, c is an empirical function and $F_H, c_p, \rho, k_t, g, H,$ and ν are the heat flux across the interface, the specific heat capacity, the density, the molecular diffusivity of heat, gravitational acceleration, layer height, and the kinematic viscosity, respectively. For large *Ra* convection, the heat flux, F_H, should show no dependence on layer height, *H*, because fluid parcels near the top of the convecting layer should only be influenced by parcels nearby rather than parcels at the bottom of the layer. Thus, η is traditionally chosen as 1/3 to remove dependence of F_H on *H* [*Turner*, 1965].

For double diffusive convection, *Turner* [1965] showed that c was a function of the density ratio, $c(R_\rho)$. Two formulations of this variable are commonly used currently. Based on existing laboratory studies, *Kelley* [1990], K90, proposed the empirical function,

$$c\left(R_\rho\right) = 0.0032 e^{\left(\frac{4.8}{R_\rho^{0.72}}\right)}. \tag{4}$$

A more recent 3-D direct numerical simulation discussed in *Flanagan et al*. [2013], F13, found the following relation to be more accurate:

$$c\left(R_\rho\right) = 0.0157 + 0.0505\left(R_\rho - 1\right)^{-1.24}. \tag{5}$$

With $\eta = 1/3$, the heat flux can be computed by what is commonly referred to as the 4/3rd laboratory flux law:

$$F_H = c\left(R_\rho\right)\rho c_p \left(\frac{g k_t^2 \alpha}{\upsilon}\right)^{1/3} (\Delta T)^{4/3}. \tag{6}$$

However, *Flanagan et al*. [2013] note that (5) corresponds to the use of the 1/3rd exponent in (3) which they claim represents their experiment poorly and suggest a downward revision. *Kelley et al*. [2003] also

questions the use of $\eta=1/3$ in (3), but suggests it be retained until observational evidence indicates otherwise. A recent examination of a diffusive convective staircase in Lake Kivu, Africa yields $\eta=0.2$ [*Sommer et al*., 2013a]. However, other laboratory and numerical simulations of single-component convection suggest a more moderate downward revision than *Sommer et al*. [2013a]. While a thorough review of single-component Rayleigh-Bernard convection literature is outside the scope of this introduction, *Niemela et al*. [2000] show that $\eta=0.31$ provides the best fit to their data and *Kerr* [1996] finds $\eta=0.29$ provides the most accurate representation. Despite somewhat conflicting results, recent literature has provided mounting evidence that a downward revision of η is necessary.

The presence of diffusive convective thermohaline staircases in the Canada Basin of the Arctic Ocean has been documented since the 1960s [*Neshyba et al*., 1971]. *Padman and Dillon* [1987] studied it in more detail with a suite of microstructure measurements made during AIWEX and *Timmermans et al*. [2008] with Ice-Tethered Profilers (ITPs) during the 2000s. *Padman and Dillon* [1987] found heat fluxes to be low, around 0.1 Wm^{-2} and that the 4/3rd laboratory flux laws agreed to within a factor of two with the molecular heat fluxes across the interface. *Timmermans et al*. [2008] found slightly higher heat fluxes averaging 0.22 Wm^{-2}, and attributed this to an increase in the AW temperature maximum in the Canada Basin over the previous 20 years. They also made a comparison to temperature data from a single microstructure profile reported by *Rainville and Winsor* [2008] and found similar agreement to the results presented in *Padman and Dillon* [1987]. Detailed spatial coverage of the staircase is presented for the first time in *Timmermans et al*. [2008], where the ITPs revealed that a thermohaline staircase was present between 200 and 300 m depths in 95% of the profiles made over the deep part of the Canada Basin.

The existence of thermohaline staircases in the Eurasian Basin appears more sporadic. A staircase similar to the one found in the Canada Basin was reported by *Sirevaag and Fer* [2012] during two different microstructure field experiments in the AB in 2008. Polyakov et al. [2012] used data from a McLane Moored Profiler attached to a bottom mooring on the Laptev Sea slope to report on a thermohaline staircase quite different than ones previously reported in the Arctic Ocean [*Padman and Dillon*, 1987; *Timmermans et al*., 2008; *Sirevaag and Fer*, 2012]. The Laptev slope staircase was comprised of thicker (O(1) m) interfaces and (O(10) m) layers and purportedly much higher heat fluxes, O(1) Wm^{-2}, than previous studies. The *Polyakov et al*. [2012] heat fluxes are derived using the *Kelley* [1990] formulation and are significantly higher than other results due to much greater ΔT, 0.25°C, and much lower R_ρ, 1.8–2.4.

None of the Arctic observations reviewed above were designed to resolve the heat fluxes through the thermohaline staircases. This paper discusses observations purposely designed to improve on previous tests of the validity of the 4/3rd laboratory flux law heat flux parameterizations applied to oceanographic measurements made in the Amundsen Basin of the Arctic Ocean. Here, double diffusive heat fluxes predicted by laboratory flux law parameterizations are compared to heat fluxes calculated from direct temperature microstructure measurements: conductive, molecular fluxes in the interfaces, and the turbulent nonconductive heat fluxes in the convective layers. Furthermore, since temperature gradient spectra in the interfaces have not been previously reported, the temperature gradient spectra and the dissipation rate of thermal variance are presented and contrasted between the interfaces and the layers. The value of the convective exponent, η, in (3) is explored, and these results are discussed in terms of their basin-wide implications. Data collection and processing methods are presented in section 2. Results are given in section 3. Conclusions and departures from previous literature are discussed in section 4.

2. Data and Methods

2.1. Overview and Hydrography

Observations were made from a drifting ice camp, Barneo, in April 2013. The measurement period began on 11 April 2013 when the camp was located at 89°33′N, 87°24′W and ended on 19 April 2013 at 89°07′N, 62°18′W after the camp drifted along the Eurasian flank of the Lomonosov Ridge (Figure 1). Over this time, a total of 42 casts down to 350 m were made through a 51 cm hole in the 1.5 m thick sea ice. The instrument package consisted of a Seabird (SBE) 19+ CTD attached to a Rockland Scientific International Microrider (RSI MR-1000) internally recording microstructure instrument. Sensors on the Microrider included two shear probes to measure microscale shear perturbations as well as two Thermometric FP07s thermistors to measure microscale temperature fluctuations. The fast-response thermistor signal was preemphasized in a

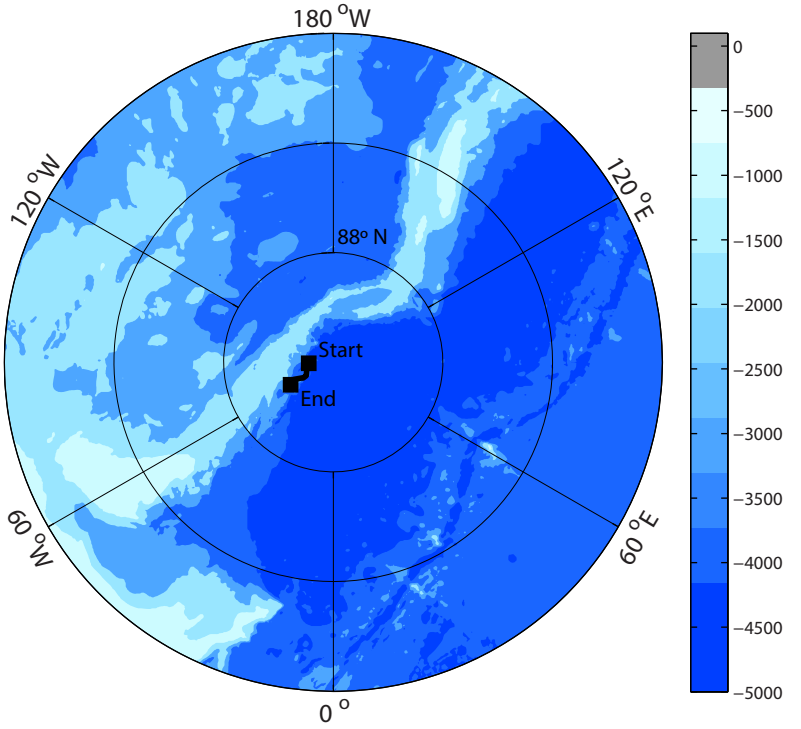

Figure 1. A map of the drift. The camp drifted mainly south along the flank of the Lomonosov Ridge.

separate channel for high-resolution temperature gradient measurements, crucial for dissipation rate calculations. In this study, only dissipation rates inferred from FP07 measurements are reported. The instrument package was lowered with a winch at a speed of 20–25 cms^{-1}. The SBE 19+ sampled at a rate of 4 Hz while the RSI MR-1000 sampled at 512 Hz. Manufacturer specified instrumental errors on the SBE 19+ are 0.005°C in temperature and 0.0005 Sm^{-1} in conductivity. All salinity data discussed hereafter are derived from the SBE 19+. Due to sensor drift typical of fast-response thermistors, temperature data from the FP07s were calibrated against the more accurate SBE 19+ measurements using a running third-order polynomial fit over 10 cm sections of data.

Bulk T-S properties changed little over the course of the drift, implying small horizontal gradients. A sample profile of T and S versus depth from the midpoint of the drift is shown in Figure 2. AW temperature maxima occurred at roughly 300 m depth and ranged between 1.1 and 1.2°C, while AW salinity maxima occurred at the same depth and were roughly 34.8. The insets show details of interfaces and layers from the portion of the water column containing a thermohaline staircase. The staircase nominally begins at 150 m depth and extends to 230 m depth although there is variability between profiles. Often, interfaces and layers appear in the region directly above the AW temperature maximum as well.

Mixed layer depths were small throughout the drift, relative to an average springtime value in the Eurasian Basin of 71 m [*Peralta-Ferriz and Woodgate*, 2015]. Mixed layer depth was calculated as the depth at which $\Delta\rho > 0.1$ kgm^{-3} relative to the uppermost measurement. The mean mixed layer depth was 22 m. A roughly isothermal layer near the freezing point, $T = -1.6$°C, was present down to approximately 60 m during the course of the experiment. The analysis presented in this paper will focus mainly on aspects of the thermohaline staircase between 150 and 250 m depths. Density ratio used in the calculation of (4) and (5) is obtained using ΔT and ΔS, the temperature and salinity jumps across the interfaces, respectively. Mean staircase parameters were: $\Delta T = 0.026$°C, $\Delta S = 0.007$, $h = 0.1$ m, $H = 1.33$ m, $R_\rho = 3.45$, and $Ra = 1 \times 10^9$, where h is the height of the interface. Histograms of these parameters derived from 360 interfaces are shown in Figure 3.

2.2. Spectral Analysis

Dissipation rate of thermal variance is obtained by spectral analysis of well-resolved temperature gradient spectra, both in the turbulent convective layers and the quiescent interfaces. A comparison of spectral

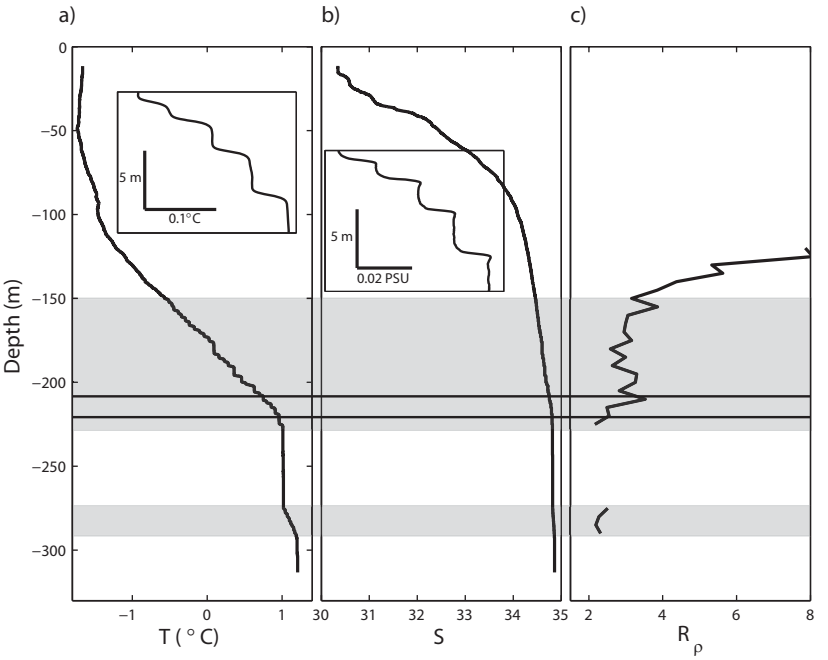

Figure 2. Sample temperature, salinity, and R_ρ profiles from the SBE 19+. R_ρ is based on 5 m linear fits to T and S. Gray shading highlights depths where interfaces are found. The salinity scale makes resolution of individual interfaces difficult. Insets in temperature and salinity are shown.

levels and dissipation rates in the diffusive convective interfaces and layers has not been previously reported. Furthermore, measurements of turbulent heat flux from microstructure profiling relies on the eddy diffusivity of heat, K_T, which is related to the dissipation rate of thermal variance, χ. The latter is measured by integrating wavenumber spectra of temperature gradient. The details of the calculations are summarized in the following. Frequency spectra of temperature gradient were calculated from the high-resolution FP07 data extracted from the homogeneous layers and from the high gradient interfaces in the thermohaline staircase. Only interfaces thicker than 10 cm were used in spectral calculations to insure a

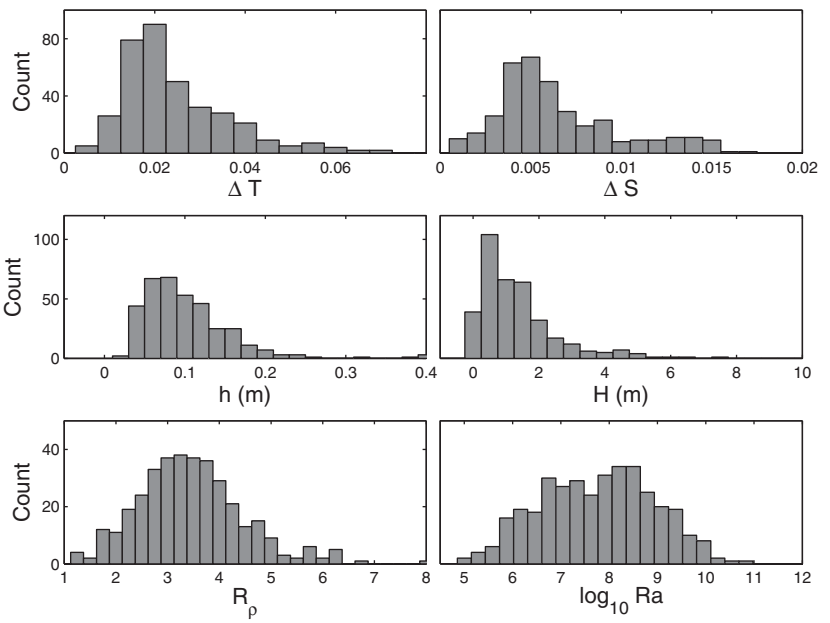

Figure 3. Histograms of ΔT, ΔS, h, H, R_ρ, and Ra are shown using data from 360 interfaces.

reasonable spectrum was resolvable. Extracted temperature gradient segments were detrended by removing the mean temperature gradient calculated from a linear fit in temperature-depth space and then windowed using a 50% Tukey window. Hanning, Hamming, and Bartlett windows were also tested and yielded comparable results. A Tukey window was chosen since it provided roughly 10% smaller (i.e., conservative) values of χ. Layer spectra were computed using Welch's modified periodogram if $H > 1$ m ($\sim$ 4 s of data). A standard periodogram if $H < 1$ m, since averaging the shorter segments changes induces unrealistic values at the lowest frequencies. When the Welch's method was applied, each layer was split into 8, 50% overlapping segments. Individual spectra of the subsegments were calculated and then averaged together to calculate the spectrum for the layer.

Due to the smaller data segments of the interfaces, 0.3–0.5 s of data, interface spectra were computed using a standard periodogram. No spectral content at frequencies greater than 50 Hz was used and typically the temperature gradient spectra in both layers and interfaces reached the diffusive roll-off portion, e.g., the part of the spectrum where molecular diffusion takes over, at frequencies much lower than 50 Hz. The attenuation of the signal due to the glass bead around the thermistor is accounted for using the *Gregg and Meagher* [1980] formulation, $H^2(f) = \left(1 + (f/f_c)^2\right)^{-2}$, where $f_c = 1/(2\pi\tau W^{-.32})$, $\tau = 12$ ms, and W is the profiling speed. This correction was applied in the frequency domain. Frequency spectra were then converted into wavenumber spectra by dividing by the profiling speed of the instrument. For the wavenumber ranges typically analyzed in this data set, the correction for the time response results in only a modest recapture of the lost variance.

The dissipation rate of thermal variance, χ, is computed as

$$\chi = 2k_t < 3\left(\partial T'/\partial z\right)^2 > . \tag{7}$$

In (7), $\left(\partial T'/\partial z\right)^2$ represents microscale temperature gradient variance, and is obtained by integrating the spectra to a cutoff wavenumber at which the noise begins to dominate. A noise spectrum for temperature gradient spectra was created by averaging the most quiescent (lowest fifth percentile) sections of individual profiles, identical to the method presented in *Peterson and Fer* [2014]. Integrating the noise spectra out to 100 cpm, roughly the highest cutoff wavenumber for integration used in this study, reveals a noise floor in χ of O(10^{-12})°C^2 s^{-1}. The factor of 3 in (7) follows from the assumption of local isotropy. It is unclear whether the isotropic assumption is valid within the high gradient interfaces and is therefore excluded from interface χ estimates (i.e., we exclude the factor of 3 in the interfaces, assuming that $\partial T'$ is relevant only in the z direction). However, a recent numerical simulation in a low R_ρ environment suggests that isotropy is reduced, but not entirely absent, when double diffusive processes are dominant [*Flanagan et al.*, 2014]. Full isotropy is assumed (e.g., a factor of 3) for χ estimates within the homogeneous convecting layers. For the calculation of χ across interfaces and layers, the cutoff wavenumber was chosen following the maximum likelihood approach of *Ruddick et al.* [2000], where a cutoff wavenumber was estimated by integrating the temperature gradient spectrum out to the highest wavenumber where the value of the spectrum was 1.5 times higher than the value of the noise spectrum at the same wavenumber. The curve fits to theoretical Kraichnan or Batchelor scalar turbulence spectra [*Batchelor*, 1959; *Kraichnan*, 1968] via this method also allow us to indirectly infer ε without shear probes. A recent underwater glider based study highlights the applicability of this method by comparing concurrent temperature and shear microstructure measurements [*Peterson and Fer*, 2014]. For 85% of their data, Peterson and Fer found that shear probe-derived dissipation and the *Ruddick et al.* [2000] curve-fitting method agreed to within a factor of 2.8, with better agreement at lower turbulence levels. Values of ε reported in section 3.4 are all inferred from the temperature gradient spectra measured by the FP07s.

2.3. Heat Flux

Heat flux calculations are made in the convective layers and interfaces. In the interfaces, we obtain the conductive heat flux using the molecular diffusivity of heat and standard Fickian diffusion,

$$F_H = -\rho c_p k_t \frac{\partial T}{\partial z}. \tag{8}$$

We discuss methods for calculating interfacial $\frac{\partial T}{\partial z}$ in section 3.1. In the turbulent layers, we rely on the Osborn-Cox (OC) model,

$$K_T = \frac{\chi}{2\langle \frac{\partial T}{\partial z} \rangle^2}, \quad (9)$$

to calculate an eddy coefficient for thermal diffusivity in the layers, and then compute the turbulent heat flux in the convective layer using (8) [*Osborn and Cox*, 1972]. In the application of (8), we use K_T (instead of k_t) and use the background temperature gradient from the sorted temperature in each layer. The OC model cannot be used in the interfaces since molecular diffusion determines the heat flux.

3. Results

3.1. Interface Structure

The 360 interfaces included in this analysis were selected visually. The initial visual selection insures that only interfaces free of unusual disturbances such as inversions and spikes are used, as these complicate temperature gradient calculation. Once the interface is chosen visually, the beginning of the segment is determined as the first point where low-pass filtered (10 Hz) temperature gradient, $\partial T/\partial z$, increases beyond twice the large-scale background value (0.02°Cm^{-1}), or $\partial T/\partial z > 0.04$°Cm^{-1}. Similarly, the end of the interface segment is chosen as the next point in the segment where $\partial T/\partial z$ drops below 0.04°Cm^{-1}. This results in a set of interfaces that appear primarily laminar, e.g., relatively smooth. However, an examination of the "laminar" interfaces in depth versus $\partial T/\partial z$ plots reveals a variety of structures and forms. The complicated structure of interfaces when viewed in temperature gradient-depth space reveals the challenges associated with calculating temperature gradient across an interface. Four interfaces that appear smooth when viewed in temperature-depth spaces are shown in Figures 4a–4d (left). The same interfaces are shown in temperature gradient-depth space in Figure 4a–4d (right). Temperature gradient calculated in three different ways are illustrated by the vertical lines. A linear fit across the interface in temperature-depth space, a linear fit across the middle 50% of the interface (following *Sommer et al*. [2014]), and the maximum temperature gradient measured by the FP07 across the interface are all used. The maximum temperature gradient recorded by the FP07 is often 2–6 times higher than values provided by the other methods. Through equation (8), this can have a similar effect on interfacial heat flux.

The model proposed by *Linden and Shirtcliffe* [1978] assumes a constant temperature gradient across the core of an interface. Their Figure 1 shows a theoretical interface in temperature-depth space. The same interface shown in temperature gradient-depth space would resemble a boxcar function, with a discontinuity necessary to reach the constant core temperature gradient at the layer-interface junction. Real, physical, oceanic interfaces are unlikely to have this idealized structure. We choose to define "cores" as the region where the temperature gradient lies within 10% of the maximum temperature gradient measured by the FP07. 85% of interfaces have cores that compose less than 30% of total interface thickness and 55% of interfaces have cores that compose less than 20% of total interface thickness. For the interfaces analyzed, mean core thickness was 1.8 cm, compared to a mean interface height of 10 cm. A comparison between the 30 Hz low-pass and raw data reveals that the interface cores are largely unaffected by high wavenumber instrument noise.

For most of the density ratio values observed here, a stable diffusive core exists near the nominal middle of the interface where the heat transport is purely molecular [*Worster*, 2004; *Sommer et al*. 2014]. The margins of the interface outside the core must present a mix of molecular and convective diffusion and consequently, a higher diffusion coefficient than purely molecular. And to the degree, a profile is representative of quasi steady state heat flux through the interface, the minimum diffusion coefficient, i.e., molecular $= k_t = 1.4 \times 10^{-7}$ m^{2}s^{-1}, must be associated with the maximum temperature gradient. By this argument, using molecular diffusivity and the maximum temperature gradient recorded by the FP07 should provide an accurate measure of heat flux in the interface. This method has been previously reported in both *Sirevaag and Fer* [2012] and *Sánchez and Roget* [2007]. The mean maximum interfacial temperature gradient is 0.6°Cm^{-1}. The value shown in Figure 4d is 10 times this value, lending confidence to the ability of the FP07s to adequately capture the maximum temperature gradient within the interface core.

3.2. Comparison With the 4/3rd Flux Law

Conductive heat flux, $F_{H(MOL)}$, across an interface is calculated using equation (8), molecular diffusivity k_t, and $\frac{\partial T_{MAX}}{\partial z}$, the maximum temperature gradient recorded by the thermistors in the interface. This flux is

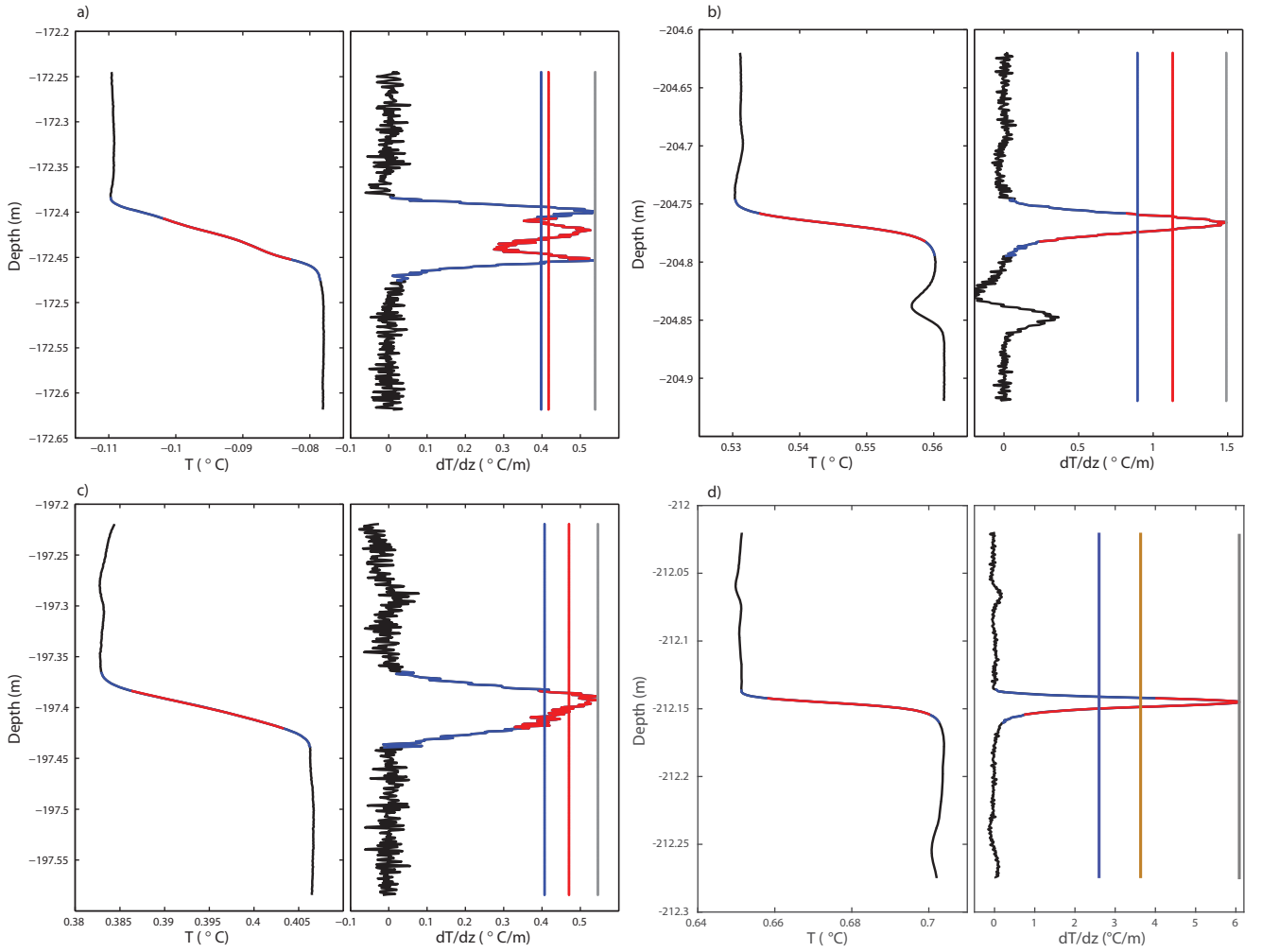

Figure 4. Temperature and temperature gradient data shown in this figure are taken from the FP07s. (a)–(d) Represent four laminar appearing interfaces that look relatively similar in temperature-depth space but look quite different in temperature gradient-depth space. Data included in interface calculations, i.e., the segment determined by the algorithm in section 3.1, is shown in blue. The middle 50% of the interface is shown in red. The three vertical lines in the right subplots represent different ways to calculate temperature gradient. A linear fit to the middle 50% of the interface is shown in red, a linear fit to the interface is shown in blue, and the maximum gradient in the interface segment is shown in gray.

compared to the 4/3rd flux law estimates of both *Flanagan et al*. [2013] and *Kelley* [1990], $F_{H(F13)}$ and $F_{H(K90)}$, shown in equation (6). Turbulent heat fluxes in the layers derived from the OC model will be discussed in section 3.4. Both the laboratory experiments of *Kelley* [1990] and the DNS of *Flanagan et al*. [2013] let their experiments reach an equilibrium state before reporting results. For this reason, we have chosen to exclude the thickest and thinnest interfaces from this analysis. For $F_{H(MOL)}$, only the interfaces with thickness in the 10th–90th percentile range are used, corresponding to interface height, h, between 4.7 and 16.3 cm, reducing the analyzed number of interfaces to 287.

$F_{H(MOL)}$ is well-correlated with both the *Kelley* [1990] and *Flanagan et al*. [2013] formulations of the 4/3rd laboratory flux law. A scatter plot of $F_{H(MOL)}$ versus both $F_{H(F13)}$ and $F_{H(K90)}$ is shown in Figure 5. We report the 24 hour-averaged values of each quantity in Figure 5 as well since the recent numerical simulation of *Flanagan et al*. [2014] suggests that time averaging reduces measurement uncertainties. The correlations are slightly higher with *Flanagan et al*. [2013] than *Kelley* [1990], $r = 0.74$ versus $r = 0.70$. Averaged across all interfaces examined, mean heat flux values are remarkably consistent, indicating the continued utility of the 4/3rd laboratory flux law parameterization. Mean $F_{H(MOL)}$ equals 0.33 Wm^{-2}, roughly 55% higher than $F_{H(F13)}$ (0.21 Wm^{-2}) and 100% higher than $F_{H(K90)}$ (0.16 Wm^{-2}). Unfortunately, we only have a small number of interfaces where $R_\rho > 4$, the value at which $F_{H(F13)}$ and $F_{H(K90)}$ really start to diverge [see *Flanagan et al*., 2013, Figure 2b]. When only interfaces where $R_\rho > 4$ are examined, $F_{H(F13)}$ appears to work much better than $F_{H(K90)}$ in comparisons with $F_{H(MOL)}$. The correlation coefficient, r, is only 0.01 higher but heat fluxes are

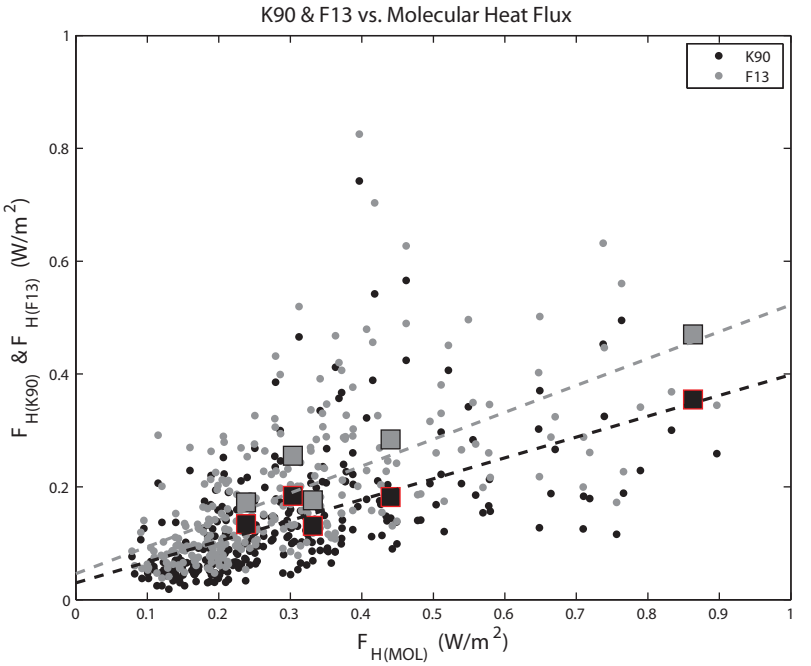

Figure 5. $F_{H(K90)}$ (black) and $F_{H(F13)}$ (gray) versus $F_{H(MOL)}$ are shown. 24 hour-averaged values are given by the large squares.

much closer in magnitude for this range of R_ρ. $F_{H(K90)}$ equals 0.09 Wm^{-2}, while $F_{H(F13)}$ equals 0.14 Wm^{-2} compared to $F_{H(MOL)}$ equal to 0.27 Wm^{-2} (not shown). This highlights the improvement of (5) compared (4) when dealing with higher R_ρ. It is possible that the scatter in Figure 5 can be explained by the oscillating nature of the instantaneous heat flux through a single interface. We refer the reader to Figure 2a of *Flanagan et al*. [2013]. Their DNS shows that the staircase reaches a state of "quasi-equilibrium." Thus, while $F_{H(MOL)}$ could represent the instantaneous flux, $F_{H(F13)}$ might better represent a time-averaged flux through an interface not captured in the microstructure measurements. This agrees qualitatively with results presented in *Worster* [2004] that fluxes through interfaces are inherently time-dependent.

3.3. Ra Versus Nu Scaling

Formulations of the 4/3rd flux laws are based on equations (1–3). This relationship implies that nondimensional heat flux, *Nu*, is equal to the product of a function, *c*, of density ratio, R_ρ, and a *Ra* power law with exponent η. Previous results have suggested $\eta = 1/3$ to remove the *H*, layer height, dependence in the 4/3rd flux law (6) based on theories of single-component convection and a simple scaling argument. Although *Kelley* [1990] suggested a downward revision of this exponent, he argued that it should remain 1/3 until some experimental evidence showed otherwise. A recent study of DDC in Lake Kivu, Africa [*Sommer et al*., 2013a] found evidence of $\eta = 0.2$ which they argue would require substantial downward revision of heat fluxes calculated using the extant 4/3rd flux laws for certain values of *Ra*. However, the authors considered only one power law fit (their Figure 9a) and make no mention of the values of the correlation coefficient for their η estimation. The relationship is undoubtedly statistically significant as evidenced by the bootstrapping shown in their Figure 9b but examining their Figure 9a, it appears that $\eta = 1/3$ could provide a fit as reasonable as $\eta = 0.2$.

The same relationship from this data set is shown in Figure 6. *Nu* is calculated in (1) using $F_{H(MOL)}$ as described in the previous section. A power law fit to the relationship reveals $\eta = 0.29$ and the correlation between *Ra* and *Nu* is high, $r = 0.74$. We have chosen to use a parametric Kendall rank-type correlation since it can better detect nonlinear relationships [*Kendall*, 1938]. Performing the power law fit for 500 bootstrapped samples gives a 95% confidence interval error estimate (shown in brackets) such that $\eta = 0.29$ [0.28 0.31] [*Efron and Gong*, 1983]. The use of a Deming regression, which assumes equal error variance in

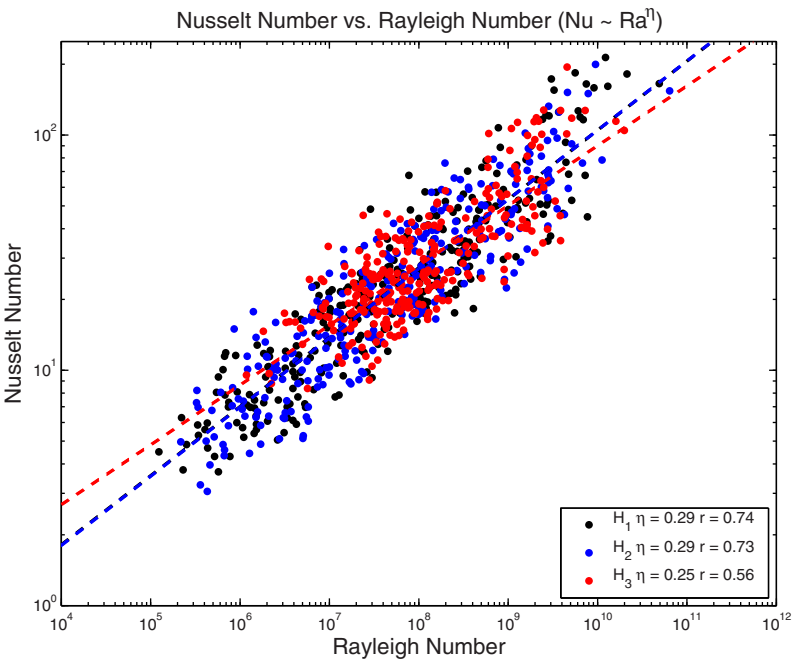

Figure 6. A plot of *Nu* versus *Ra* for different methods of *H* calculation. Dashed lines show power law fits to the relationship. *Nu* is calculated as (2) where $F_H = F_{H(MOL)}$, while *Ra* is calculated as (3). H_1 (in black) $= H_{lower} + h$, H_2 (in blue) $= H_{upper} + h$ and H_3 (in red) $= (H_{lower} + H_{upper} +)/2$. Correlations and η values are given in the legend. The lack of points at the lower *Ra* range for H_3 due to averaging appears to bias the power law fit low.

both variables and provides another error estimate, gives a very similar answer, $\eta = 0.30$ [0.28 0.32] [*Deming*, 1943].

This relationship appears sensitive to how *H*, layer height, is defined. *Sommer et al*. [2013a] calculate $H = (H_{upper} + H_{lower} + h)/2$ where H_{upper} is the layer height above the interface, H_{lower} is the layer height below the interface, and *h* is the interface thickness. In this study, *H* is chosen as the layer below the interface, but we will now investigate the sensitivity of our results to how *H* is chosen. The relationship in (1) is tested using three separate definitions of *H*. $H_1 = H_{lower} + h$, $H_2 = H_{upper} + h$ and $H_3 = (H_{lower} + H_{upper} + h)/2$. The coefficient, η equals 0.29 [0.28 0.31] for H_1 and H_2, and 0.25 [0.23 0.28] for H_3. The Kendall rank-type correlations are $r = 0.74$ for H_1, $r = 0.73$ for H_2, and $r = 0.56$ for H_3. The above values are given using only the 10th–90th percentile range in interface thickness, however, the relationship is robust to the inclusion of all interfaces, with $\eta = 0.29$ [0.27 0.30] for H_1 and H_2 and $\eta = 0.24$ [0.21 0.26] for H_3, but lower correlations ($r = 0.66$, 0.64, 0.45, respectively). In Figure 6, the effect of collapsing Rayleigh number space is clear. Although the H_3 values populate the same envelope as H_1 and H_2, η is biased low since there are fewer values at the extreme ends of Rayleigh number space. While all three choices of *H* are physically reasonable, H_3 does not appear to be a good choice for our data set since there is no statistically significant relationship between H_1 and H_2 in our data set ($r = 0.01$ and $p > 0.85$), and the error bars on η estimates are roughly 50% larger than when using H_1 or H_2.

However, we must also account for the inclusion of $c(R_\rho)$ in (3). Because both (4) and (5) are based on the assumption that $\eta = 1/3$, we have chosen to perform the analysis above in bins of varying R_ρ following *Sommer et al*. [2013a]. Individual regressions are performed for 0.5 width bins of R_ρ from 2 to 5 for all three choices of *H* listed above. The bins contain the following number of interfaces, respectively: [30, 52, 57, 58, 37, 14]. These results are shown in Figure 7. Error bars shown are based on 95% confidence intervals from the use of a Deming regression. We have chosen to show these since they are more conservative (slightly larger) than the error bars determined through the bootstrap technique. While there appears to be a weak dependency of η on R_ρ (decreasing with increasing R_ρ), the range in R_ρ is too narrow and the error bars too large to be conclusive. This analysis suggests that our regression results from Figure 6 are not biased by the dependency of regressors on R_ρ. The mean value of η calculated this way agrees with the calculations in the

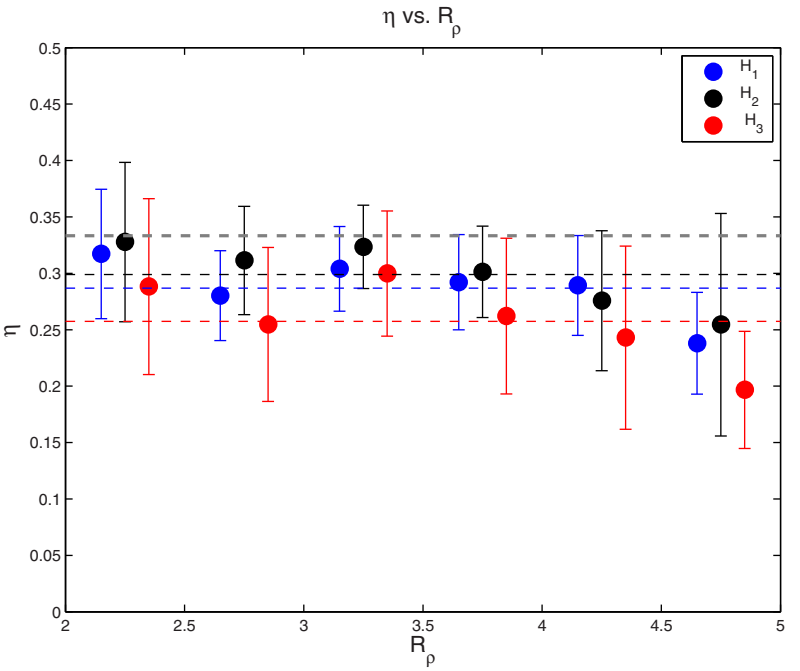

Figure 7. Plot of η versus R_ρ. Circles are shown for different values of H. R_ρ is shown in 0.5 width bins from 2 to 5. Error bars are the 95% confidence intervals based on the Deming regression. We have chosen to show the error bars from the Demming regression instead of the bootstrap because they are slightly larger Dashed blue, black, and red lines show the mean value of η for the three different choices of H. Dashed gray line is the canonical $\eta=1/3$. Mean values of η for each choice of H are identical with the first and last bins removed, i.e., only considering $2.5 < R_\rho < 4.5$.

previous two sections. For H_1, $\eta = 0.29$, for H_2, $\eta = 0.30$, and for H_3, $\eta = 0.26$. Not surprisingly, there is substantial bin to bin variability due to the smaller number of interfaces used. The mean values of η for different choices of H are identical with the first and last bins removed, i.e., only considering $2.5 < R_\rho < 4.5$.

There is support in the single-component convection literature of a downward revision of η for the Ra ranges analyzed in our data set, although this is still an area of extensive research. Direct numerical simulations of single-component convection have suggested that $\eta = 2/7 \sim 0.29$, very close to our values, might be the most appropriate choice [*Kerr*, 1996]. *Kelley* [1990] proposes a similar exponent. A laboratory study of single-component thermal convection by *Niemela et al.* [2001] found $\eta = 0.31$ over 18 orders of magnitude in Ra. If a downward revision of η is necessary, then heat fluxes should be slightly dependent on H. Regardless, the reintroduction of H into (6) changes heat flux values very little, as $H = 1.36$ m and $\eta = 0.29$ results in heat fluxes only 4% lower than predicted by the current flux laws. However, recalculating $F_{H(F13)}$ with $\eta = 0.29$ gives a mean interfacial heat flux of 0.36 Wm^{-2}, very close to the mean value of $F_{H(MOL)}$. A similar plot to Figure 5 is shown in Figure 8 but with $F_{H(F13)}$ calculated using $\eta = 0.29$ instead of $\eta = 1/3$. $\eta = 0.29$ is only applied to $(\alpha\Delta T)^{1+\eta}$, as this is the form presented in *Flanagan et al.* [2013] (see their equation (1)). Color-filled squares are averaged values binned by R_ρ ranging from 2 to 5 in 0.25 width bins. Note the nearly 1 to 1 correspondence between values for $R_\rho \geq 3$. We see some disagreement at low R_ρ. This may be related to the fact that possibility of entrainment of fluid from the interface core is not represented in the calculation of $F_{H(MOL)}$. The recent numerical simulation of *Sommer et al.* [2014] reveals that mixed layer turbulence was only able to entrain interfacial fluid when $R_\rho < 3$.

3.4. Spectral Calculations: χ and ε

The average wavenumber spectra of temperature gradient are substantially different in the layers and in the interfaces. To ensure a reasonable interface spectrum is produced, we use a subset of the above data, consisting of 146 interfaces thicker than 10 cm to check on χ differences between layers and interfaces. χ in the interfaces is 20 times higher than in the layers. Values reported below are based on the maximum likelihood estimator for a lognormal distribution, with 95% confidence intervals given in brackets. In the interfaces, χ_{int} equals 6×10^{-9} C^2s^{-1} [4×10^{-9} 9×10^{-9}] and in the layers χ_{lay} equals 3×10^{-10} C^2s^{-1} [$2 \times$

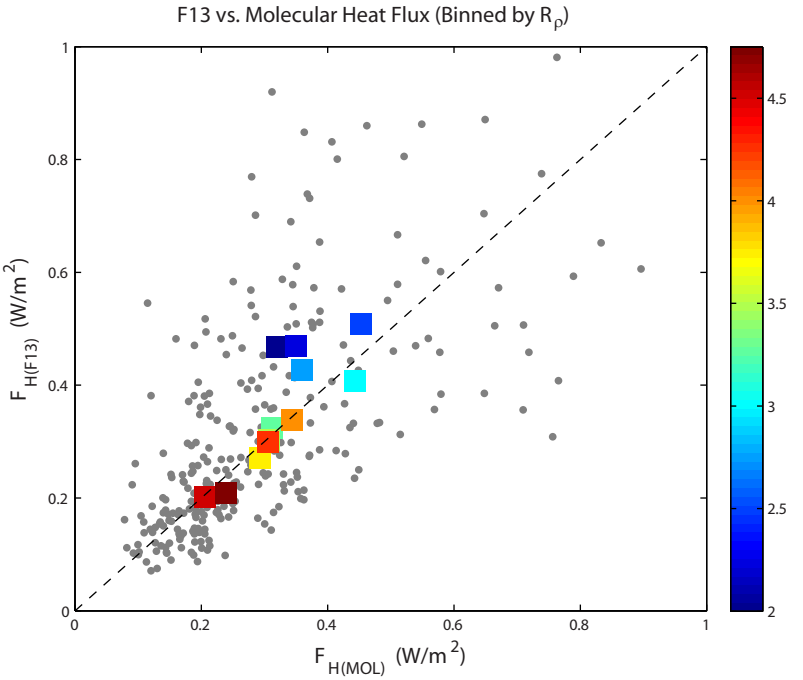

Figure 8. $F_{H(F13)}$ versus $F_{H(MOL)}$ is shown. $F_{H(F13)}$ is calculated using η equals 0.29 as determined in section 3.3. Squares represent average values of $F_{H(F13)}$ and $F_{H(MOL)}$ binned by R_ρ (color scale) from 2 to 5 in 0.25 bin widths. The dashed line shows a perfect 1 to 1 correspondence.

10^{-10} 5×10^{-10}]. This result is robust to whether or not the interface/layer pair passes the goodness-of-fit test listed in *Ruddick et al*. [2000] as well as to the choice of layer below or above the interface. Sample temperature gradient spectra and curve fits to theoretical Kraichnan spectra for an interface/layer pair are shown in Figure 9a. Admittedly, error bounds on individual interface spectra are quite large (a factor of 10) due to only 2 degrees of freedom. However, we report only χ_{int}, averaged over 146 samples, reducing the error bounds to less than a factor of 2. Averaged interfacial and layer temperature gradient spectra are shown in Figure 9b. Due to different segment lengths, individual spectra were first band-averaged to a common wavenumber vector (preserving total variance) and then averaged. The noise spectrum used in all spectral analysis is shown as well. The deviation at low wavenumber for the survey averaged interface spectra is similar to the results of *Dillon and Caldwell* [1980] for segments with low Cox number, $c = \langle \left(\frac{\partial T'}{\partial z}\right)^2 \rangle / \langle \left(\frac{\partial T}{\partial z}\right)^2 \rangle$. They argue that effects from the background temperature gradient can contaminate the low wavenumber part of the spectra, which seems especially applicable in the high gradient interfaces. In an attempt to address this problem in the interfaces, we have tried removing cubic and quadratic polynomial fits to the *dT/dz* segments before calculating spectra. Removing a cubic fit gives χ_{int} equals 3.3×10^{-9} $C^2 s^{-1}$, a factor of two lower than the reported value above, but still an order of magnitude higher than χ_{lay}.

Using the *Ruddick* et al. [2000] method also allows for the estimation of ε from the temperature gradient spectra in the interfaces and layers through curve-fitting. Only 54 of the interfaces and 65 of the layers used in the analysis pass the goodness-of-fit test. Compared to χ, the difference in ε between the interfaces and layers is much smaller and of the same order of magnitude with $\varepsilon_{int} = 5 \times 10^{-10}$ Wkg^{-1} [3×10^{-10} 7×10^{-10}] and $\varepsilon_{lay} = 3 \times 10^{-10}$ Wkg^{-1} [2×10^{-10} 4×10^{-10}]. Curve fitting to the survey-averaged spectra provides similar results for the interface but a slightly smaller $\varepsilon_{lay} = 1 \times 10^{-10}$ Wkg^{-1} [6×10^{-11} 2×10^{-10}] with error estimates providing the range of values in brackets. Given the small number of interfaces passing the goodness-of-fit test, the similarity of the result and the error bars involved, it is not possible to draw firm conclusions regarding dissipation rate of TKE. Indeed, direct calculation of ε using shear spectra in interfaces and layers is probably beyond the community's ability to resolve currently. Separation of layers and interfaces into different segments would be challenging and the calculation of ε across a 10 cm interface at typical shear-focused microstructure profiler drop rates (0.5–1 m s^{-1}) is probably not possible with only 0.1 s of data. The low ε levels expected at staircase depths in the Arctic Ocean, O(10^{-10} Wkg^{-1}), further

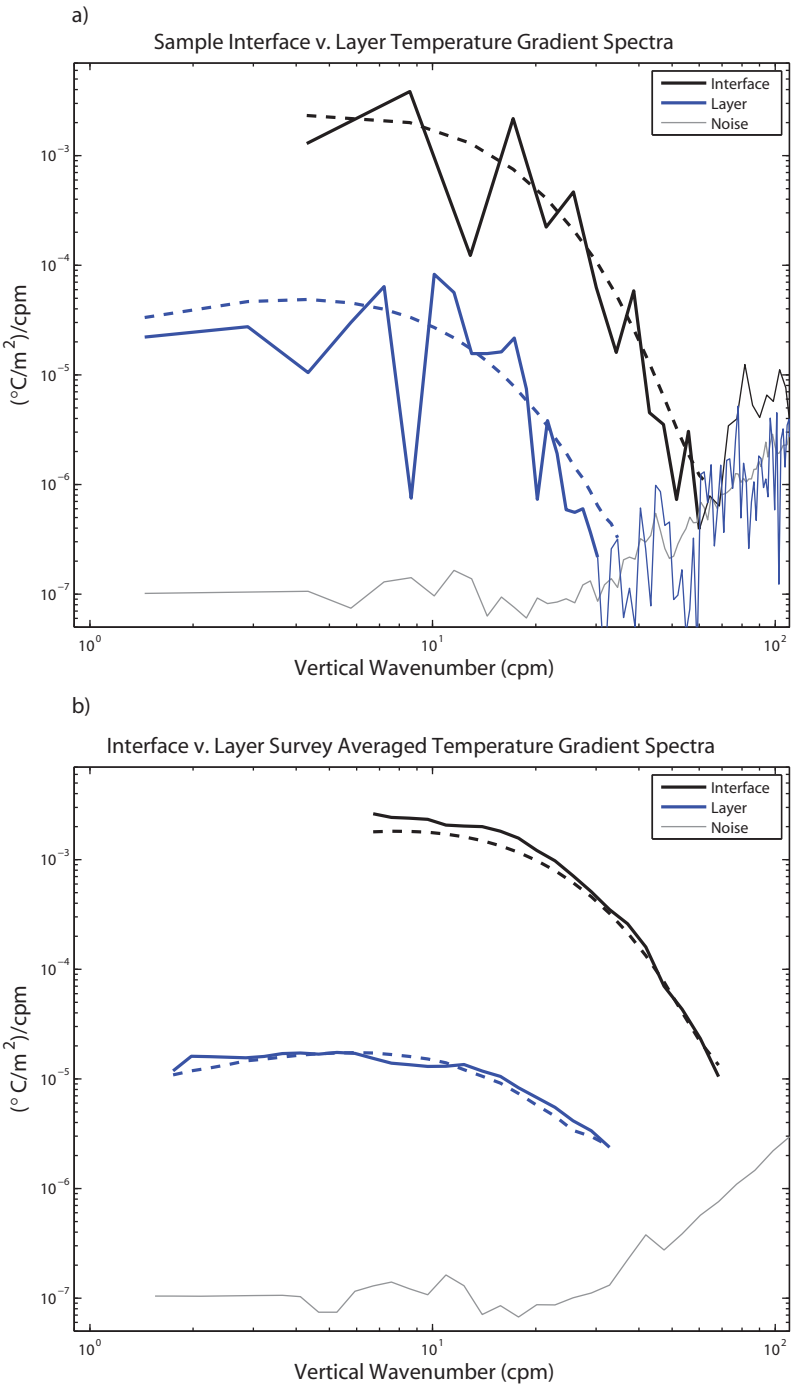

Figure 9. (a) Sample spectra are shown for an interface (black) and the layer (blue) directly below. Fits to the theoretical Kraichnan spectrum are shown in dashed. The noise spectrum for the data set is shown in gray. For this particular example, $\chi_{int} = 7 \times 10^{-9}$ C^{2}s^{-1} and $\chi_{lay} = 5 \times 10^{-10}$ C^{2}s^{-1}. (b) Survey averaged spectra are shown for interfaces (black) and layers (blue). $\chi_{int} = 4 \times 10^{-9}$ C^{2}s^{-1} and $\chi_{lay} = 3 \times 10^{-10}$ C^{2}s^{-1} for the survey-averaged spectra.

complicate this issue. *Taylor* [1988] proposed that in a uniform, steady state staircase, the buoyancy flux through the interfaces would be dissipated in the layer above, e.g., $\varepsilon = B_\rho \approx \frac{g\alpha}{\rho c_p} F_H$ as presented in *Padman* [1994]. Using $F_H = 0.33$ Wm^{-2} predicts $\varepsilon_{lay} = 4.7 \times 10^{-11}$ Wkg^{-1}, which is just outside the error bounds on ε calculated from a theoretical Kraichnan fit to the survey-averaged layer spectrum, indicating that the staircase is most likely not in equilibrium during our measurement period.

Spectral calculations made in the turbulent homogeneous layers also provide us with another method of calculating heat fluxes through the staircase through the application of (7), (8), and (9), $F_{H(OC)}$. χ is calculated from individual layer segments with spectral analysis described in section 2.2. Following both *Sirevaag and Fer* [2012] and *Sánchez and Roget* [2007], we calculate $\partial T/\partial z$ used in (9) by sorting the temperature profile through a layer and then performing a linear fit to the layer segment. Derived through this method, mean layer $F_{H(OC)} = 0.33 \pm 0.02$ Wm^{-2}, essentially identical to the value of $F_{H(MOL)}$.

Both results in ε and χ are qualitatively similar to the results presented in *Gregg and Sanford* [1987] from the salt fingering staircase east of Barbados during the CSALT experiment. They also found a nearly two order of magnitude difference in χ between layers and interfaces, $\chi_{int-CSALT} = 1.1 \times 10^{-7}$ C^{2}s^{-1} and $\chi_{lay-CSALT} = 5.7 \times 10^{-9}$ C^{2}s^{-1}, although they did find three times larger ε in the interface compared to the layer, $\varepsilon_{int-CSALT} = 4.9 \times 10^{-10}$ Wkg^{-1} and $\varepsilon_{lay-CSALT} = 1.4 \times 10^{-10}$ Wkg^{-1}. The ε values presented in *Gregg and Sanford* [1987] were computed from shear microstructure measurements, where ours were determined indirectly through curve fitting to theoretical temperature gradient spectra, which might explain the slight discrepancy. They also show that the salt fingering laboratory flux laws overestimate the buoyancy flux through an interface by two orders of magnitude compared to the microstructure measurements. While the values of ε and χ presented in this study are quite similar to the results published in *Gregg and Sanford* [1987], the laboratory flux laws in the diffusive convective regime of double diffusion seem to do a remarkable job in predicting actual interfacial heat fluxes, as shown in the previous section.

4. Discussion

Our observations of vertical heat flux through a thermohaline staircase in the Amundsen Basin of the Arctic Ocean agree well (within 55%) with parameterizations developed from theory and laboratory experiments. Assuming that the heat flux is constant through the interface, it can be calculated based on the molecular diffusivity of heat and the maximum temperature gradient measured by the thermistors to yield $F_{H(MOL)}$. The 4/3rd flux law (6) based on laboratory results and using η equal to 1/3rd produces flux estimates 55% lower than $F_{H(MOL)}$. However, changing η from 1/3rd to 0.29 in (6) based on the findings in this study results in very similar mean staircase heat fluxes of 0.36 ± 0.02 Wm^{-2} when we use the slightly modified form of $F_{H(F13)}$ reported in section 3.3. These values are consistent with turbulent heat flux, $F_{H(OC)}$, calculated through spectral analysis and the use of the Osborn-Cox mixing model. This indicates that using extant flux laws based on a higher exponent will lead to underestimates of heat fluxes due to double diffusion. Modifying the laboratory flux laws as recommended above results in only a 10% difference between $F_{H(F13)}$, $F_{H(MOL)}$, and $F_{H(OC)}$, and even better correspondence for $R_\rho > 3$, as shown in Figure 8. We recommend future studies use this modified version until new formulations of $c(R_\rho)$ based on a smaller value of η are derived in the laboratory or through direct numerical simulation.

If the double diffusive heat fluxes are typically this small, is this correction important? One might argue that the data set (number of interfaces) is small and 0.33 Wm^{-2} as the mean staircase heat flux is not representative, but the 287 calculated interfacial heat fluxes are lognormally distributed (not shown) and should signify a representative subset. This value is nearly the same as the value presented in *Timmermans et al.* [2008] if $\eta = 0.29$ is used instead of 1/3. If we extrapolate this result to the total area of the deep basins of the Arctic Ocean (7×10^{12} m^3), this results in total vertical heat loss from the AW of 2.3 TW, or roughly 6% of the total heat transported into the Arctic Ocean through Fram Strait (41 TW). If we assume that $\eta = 1/3$ is correct, then, double diffusion likely results in 1.4 TW of vertical heat loss from the AW. While a difference of 1 TW is probably not large compared to interannual variations in basin-scale budgets since it is considerably smaller than interannual variability of the AW inflow [*Schauer et al.*, 2008], it is likely significant as a long-term bias in heat flux estimates, and an effort should be made to further verify the proper choice of η. While the lack of a consistent thermohaline staircase in the Amundsen Basin limits the applicability of these results to the smooth T and S profiles often found in this region, a recent study of shear-based parameterized mixing shows comparable heat flux values [*Guthrie et al.*, 2013].

The results presented in this study differ slightly from a pair of recently published articles [*Sommer et al.*, 2013a; *Sirevaag and Fer* 2012]. From their Lake Kivu data set, *Sommer et al.* [2013a] found reasonable agreement between interfacial heat fluxes and the K90 version of (6). From their Lake Kivu data set, *Sommer et al.* [2013a] found reasonable agreement between interfacial heat fluxes and the K90 version of (6).

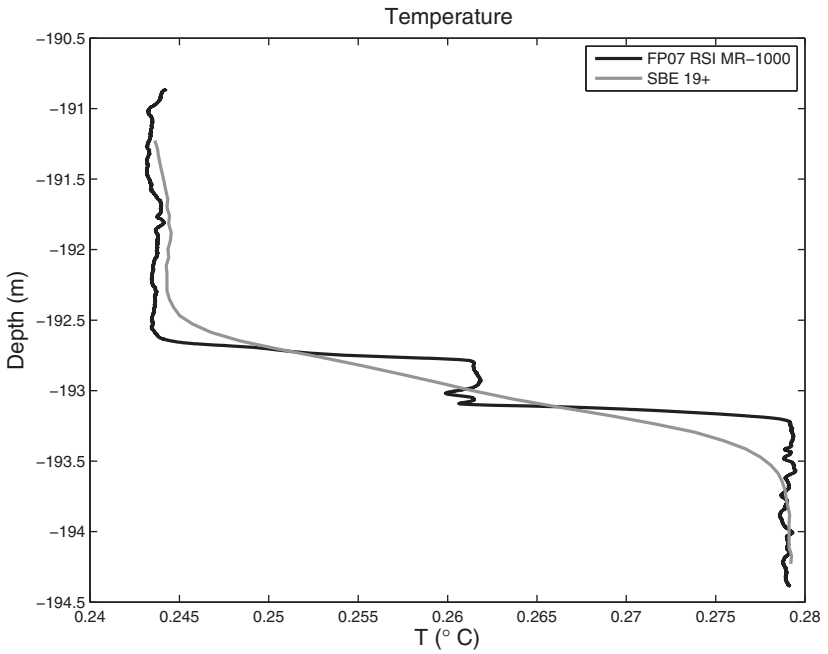

Figure 10. A sample interface is shown as seen by both the RSI MR-1000 (black) and the SBE 19+ (gray). Even though, the SBE 19+ samples at 4 Hz, compared to the 1 Hz sampling of ITPs and MMPs, it still resolves only a single interface when the MR-1000 clearly shows two.

Recalculation of the exponents presented in *Sommer* et al. [2013a] using the three different definitions of H in Ra did not change the value of η they report (J. Carpenter, personal communication, 2015). It is possible that their method of calculating molecular fluxes introduces some of the discrepancy. *Sommer et al*. [2013a] use measured $\partial T/\partial z$ at the midpoint of the interface, which could result in underestimating fluxes if maximum $\partial T/\partial z$ is not located at the exact midpoint. *Sommer* et al. [2014] use a linear fit to the middle 50% of the interface, which would result in lower values than the ones presented here as well. We also report mean ΔT 2.5 times as large as the Lake Kivu data set, 0.026°C compared to 0.01°C, which might further explain some of the differences in the comparisons of the results.

Sirevaag and Fer [2012] found that $F_{H(K90)}$ greatly overestimated $F_{H(MOL)}$ in their data sets from the AB. The disagreement between our results and *Sirevaag and Fer* [2012] can be attributed to at least two important differences between our methods. First, the instrumentation and sampling is substantially different: the faster profiling speed (0.6 m s^{-1}) and the treatment of the temperature channel of their profiler MSS-90 (difference in electronics and further lowpass filtering their data to 30 Hz, leading to smoothing on a 2 cm scale) likely limited the authors' ability to adequately resolve the temperature gradient in the 1–2 cm thick core of the interface. This would mean an underestimate in heat fluxes and explains their supposition that (6) vastly overestimated interfacial heat fluxes in their data set. Second, *Sirevaag and Fer* [2012] use ΔT from 10 cm averaged, precision CTD data (not the FP07 data at full resolution), to be consistent with the salinity jump ΔS used in staircase parameter calculations. It is highly likely that the scenario presented in the following paragraph could have affected their results by overestimating ΔT. Due to the nonlinear relationship to F_H in (6), this would significantly overestimate the heat fluxes determined through the use of the laboratory 4/3rd flux law parameterizations.

Challenges still exist in using the laboratory flux laws with CTD data, as even fast sampling, slowly profiled CTDs can erroneously show a single interface when the temperature microstructure profile reveals two. This could lead to a 100% overestimate in estimated heat fluxes. For the relatively small heat fluxes reported in *Timmermans et al*. [2008] and *Sirevaag and Fer* [2012], this is less consequential to the long-term thermodynamics because heat fluxes that small are unlikely to play any significant role in basin-scale AW heat budget considerations. However, this sampling problem could have profound impact on staircases similar to the one reported in *Polyakov et al*. [2012]. If O(0.1) m interfaces measured by the 4 Hz sampling SBE 19+ lowered at 25 cms^{-1} can be shown to consist of more than one interface in the FP07 thermistor data as in Figure 10, then it seems reasonable that the large, O(1) m interfaces measured by the 1 Hz sampling McLane

Moored Profiler data reported in *Polyakov et al*. [2012] might contain multiple smaller interfaces. In such a case, the reported large heat fluxes, 2–8 Wm^{-2}, could represent a factor of two overestimate or more.

During this drift, vertical heat fluxes from the AW core were small over the deep part of the Amundsen Basin and this suggests, as with previous studies, that most of the heat loss in the Atlantic Water layer in the Arctic Ocean must occur near the margins and over topography.

Acknowledgments

J.G. and J.M. were funded through NSF ARC-0909408 and ARC-0856330. I.F. has partly received support from the Research Council of Norway through the project "On Thin Ice: Role of Ocean Heat Flux in Sea Ice Melt" (229786/E10). We would especially like to thank Jeff Carpenter, Dan Kelley, and one anonymous reviewer for their dedication and insight. Their comments greatly improved the readability and quality of this manuscript. Andy Heiberg and Dean Stewart (NPEO team) provided excellent logistical help, while Cecilia Peralta-Ferriz offered invaluable bathymetry map guidance. The temperature microstructure and CTD data used in this article are available by e-mailing the corresponding author, J.G., at guthriej@apl.washington.edu, due to large file sizes.

References

Batchelor, G. K. (1959), Small-scale variation of convected quantities like temperature in turbulent fluid. Part 1: General discussion and the case of small conductivity, *J. Fluid Mech.*, *5*(1), 113–133, doi:10.1017/S002211205900009X.

Deming, W. E. (1943), *Statistical Adjustment of Data*, John Wiley, N. Y.

Dillon, T. M., and D. R. Caldwell (1980), The Batchelor spectrum and dissipation in the upper ocean, *J. Geophys. Res.*, *85*(C4), 1910–1916, doi:10.1029/JC085iC04p01910.

Efron, B., and G. Gong (1983), A leisurely look at the bootstrap, the jackknife, and cross-validation, *Am. Stat.*, *37*(1), 36–48.

Fer, I. (2009), Weak vertical diffusion allows maintenance of cold halocline in the central Arctic, *Atmos. Ocean. Sci. Lett.*, *2*(3), 148–152.

Flanagan, J. D., A. S. Lefler, and T. Radko (2013), Heat transport through diffusive interfaces, *Geophys. Res. Lett.*, *40*, 2466–2470, doi:10.1002/grl.50440.

Flanagan, J. D., T. Radko, W. J. Shaw, and T. P. Stanton (2014), Dynamic and double-diffusive instabilities in a weak pycnocline. Part ii: Direct numerical simulations and flux laws, *J. Phys. Oceanogr.*, *44*, 1992–2012, doi:10.1175/JPO-D-13-043.1.

Gregg, M. C., and T. B. Meagher (1980), The dynamic response of glass rod thermistors, *J. Geophys. Res.*, *85*(C5), 2779–2786, doi:10.1029/JC085iC05p02779.

Gregg, M. C., and T. B. Sanford (1987), Shear and turbulence in thermohaline staircases, *Deep Sea Res., Part A*, *34*(10), 1689–1696, doi:10.1016/0198-0149(87)90017-3.

Guthrie, J. D., J. H. Morison, and I. Fer (2013), Revisiting internal waves and mixing in the Arctic Ocean, *J. Geophys. Res. Oceans*, *118*, 3966–3977, doi:10.1002/jgrc.20294.

Kelley, D. E. (1990), Fluxes through diffusive staircases: A new formulation, *J. Geophys. Res.*, *95*(C3), 3365–3371, doi:10.1029/JC095iC03p03365.

Kelley, D. E., H. J. S. Fernando, A. E. Gargett, J. Tanny, and E. Özsoy (2003), The diffusive regime of double-diffusive convection, *Prog. Oceanogr.*, *56*(3–4), 461–481, doi:10.1016/S0079-6611(03)00026-0.

Kendall, M. G. (1938), A new measure of rank correlation, *Biometrika*, *30*, 81–93, doi:10.2307/2332226.

Kerr, R. M., (1996), Rayleigh number scaling in numerical convection, *J. Fluid Mech.*, *310*, 139–179, doi:10.1017/S0022112096001760.

Kraichnan, R. H., (1968), Small-scale structure of a scalar field convected by turbulence, *Phys. Fluids*, *11*, 945–953, doi:10.1063/1.1692063.

Levine, M. D., C. A. Paulson, and J. H. Morison (1987), Observations of internal gravity waves under the Arctic pack ice, *J. Geophys. Res.*, *92*(C1), 779–782, doi:10.1029/JC092iC01p00779.

Linden, P. F. and T. G. L. Shirtcliffe (1978), The diffusive interface in double-diffusive convection, *J. Fluid Mech.*, *87*(3), 417–432, doi:10.1017/S002211207800169X.

Neshyba, S., V. T. Neal, and W. Denner (1971), Temperature and conductivity measurements under Ice Island T-3, *J. Geophys. Res.*, *76*(33), 8107–8120, doi:10.1029/JC076i033p08107.

Niemela, J. J., L. Skrbek, K. R. Sreenivasan, and R. J. Donnelly (2000), Turbulent convection at very high Rayleigh numbers, *Nature*, *404*, 837–840.

Osborn, T. R., and C. S. Cox (1972), Oceanic fine structure, *Geophys. Fluid Dyn.*, *3*, 321–345.

Padman, L. (1994), Momentum fluxes through sheared oceanic thermohaline steps, *J. Geophys. Res.*, *99*(C11), 22,491–22,499, doi:10.1029/94JC01741.

Padman, L., and T. M. Dillon (1987), Vertical heat fluxes through the Beaufort Sea thermohaline staircase, *J. Geophys. Res.*, *92*(C10), 10,799–10,806, doi:10.1029/JC092iC10p10799.

Peralta-Ferriz, C., and R. A. Woodgate (2015), Seasonal and interannual variability of pan-Arctic surface mixed layer properties from 1979 to 2012 from hydrographic data, and the dominance of stratification for multiyear mixed layer depth shoaling, *Prog. Oceanogr.*, *134*, 19–53, doi:10.1016/j.pocean.2014.12.005.

Peterson, A. K., and I. Fer (2014), Dissipation measurements using temperature microstructure from an underwater glider, *Methods Oceanogr.*, *10*, 44–69, doi:10.1016/j.mio.2014.05.002.

Polyakov, I.V., A. V. Pnyushkov, R. Rember, V. V. Ivanov, Y.-D. Lenn, L. Padman, and E. C. Carmack (2012), Mooring-based observations of double-diffusive staircases over the Laptev Sea Slope, *J. Phys. Oceanogr.*, *42*, 95–109, doi: 10.1175/2011JPO4606.1.

Rainville, L., and P. Winsor (2008), Mixing across the Arctic Ocean: Microstructure observations during the Beringia 2005 Expedition, *Geophys. Res. Lett.*, *35*, L08606, doi:10.1029/2008GL033532.

Ruddick, B., A. Anis, and K. Thompson (2000), Maximum likelihood spectral fitting: The batchelor spectrum, *J. Atmos. Oceanic Technol.*, *17*, 1541–1555, doi:10.1175/1520-0426(2000)017<1541:MLSFTB>2.0.CO;2.

Rudels, B., E. P. Jones, U. Schauer, and P. Eriksson (2004), Atlantic sources of the Arctic Ocean surface and halocline waters. *Polar Res.*, *23*(2), 181–208.

Sánchez, X., and E. Roget (2007), Microstructure measurements and heat flux calculations of a triple-diffusive process in a lake within the diffusive layer convection regime, *J. Geophys. Res.*, *112*, C02012, doi:10.1029/2006JC003750.

Schauer, U., B.-M. Agnieszka, W. Walczowski, E. Fahrbach, J. Piechura, and E. Hansen (2008), Variations of measured heat flow through the Fram Strait between 1997 and 2006, in *Arctic-Subarctic Ocean Fluxes: Defining the Role of the Northern Seas in Climate*, edited by R. R. Dickson, J. Meincke, and P. Rhines pp. 65–85, Springer, Netherlands.

Sirevaag, A., and I. Fer (2012), Vertical heat transfer in the Arctic Ocean: The role of double-diffusive mixing, *J. Geophys. Res.*, *117*, C07010, doi:10.1029/2012JC007910.

Sommer, T., J. R. Carpenter, M. Schmid, R. G. Lueck, M. Schurter, and A. Wüest (2013a), Interface structure and flux laws in a natural double-diffusive layering, *J. Geophys. Res. Oceans*, *118*, 6092–6106, doi:10.1002/2013JC009166.

Sommer, T., J. R. Carpenter, M. Schmid, R. G. Lueck, and A. Wüest (2013b), Revisiting microstructure sensor responses with implications for double-diffusive fluxes, *J. Atmos. Oceanic Technol.*, *30*, 1907–1923, doi:10.1175/JTECH-D-12-00272.1.

Sommer, T., J. R. Carpenter, and A. Wüest (2014), Double-diffusive interfaces in Lake Kivu reproduced by direct numerical simulations, *Geophys. Res. Lett.*, *41*, 5114–5121, doi:10.1002/2014GL060716.

Taylor, J. (1988), The fluxes across a diffusive interface at low values of the density ratio. *Deep Sea Res., Part A*, *35*(4), 555–567, doi:10.1016/0198-0149(88)90131-8.

Timmermans, M.-L., J. Toole, R. Krishfield, and P. Winsor (2008), Ice-tethered profiler observations of the double-diffusive staircase in the Canada Basin thermocline, *J. Geophys. Res.*, *113*, C00A02, doi:10.1029/2008JC004829.

Turner, J. S. (1965). The coupled turbulent transports of salt and heat across a sharp density interface. *Int. J. Heat Mass Transp.*, *8*, 759–767.

Worster, M. G. (2004), Time-dependent fluxes across double-diffusive interfaces, *J. Fluid Mech.*, *505*, 287–307, doi:10.1017/S0022112004008523.